Mitochondrial Phosphopantetheinylation is Required for Oxidative Function

Pieter R. Norden[1,*], Riley J. Wedan[1,*], Jacob Z. Longenecker[1], Samuel E. J. Preston[1], Naomi Graber[1], Olivia A. Pentecost[1], Morgan Canfield[1], Elizabeth McLaughlin[1], and Sara M. Nowinski[1]

[1]Department of Metabolism and Nutritional Programming, Van Andel Institute, Grand Rapids, MI

*These authors contributed equally

Correspondence:

Sara.nowinski@vai.org (S.N.)

Abstract

4'-phosphopantetheinyl (4'PP) groups are essential co-factors added to target proteins by phosphopantetheinyl transferase (PPTase) enzymes. Although mitochondrial 4'PP-modified proteins have been described for decades, a mitochondrially-localized PPTase has never been found in mammals. We discovered that the cytoplasmic PPTase aminoadipate semialdehyde dehydrogenase phosphopantetheinyl transferase (AASDHPPT) is required for mitochondrial respiration and oxidative metabolism. Loss of AASDHPPT results in failed 4'-PP modification of the mitochondrial acyl carrier protein and blunted activity of the mitochondrial fatty acid synthesis (mtFAS) pathway. We found that in addition to its cytoplasmic localization, AASDHPPT localizes to the mitochondrial matrix via an N-terminal mitochondrial targeting sequence contained within the first 13 amino acids of the protein. Our data show that this novel mitochondrial localization of AASDHPPT is required to support mtFAS activity and oxidative function. We further identify two variants of uncertain significance in *AASDHPPT* that are likely pathogenic in humans due to loss of mtFAS activity.

Keywords:

Mitochondria, fatty acid synthesis, electron transport chain, reductive carboxylation, metabolism, respiration, compartmentalization, phosphopantetheine

Abbreviations:

35 4'PP – 4'-phosphopantetheine/yl, AASDHPPT – aminoadipate semialdehyde
36 dehydrogenase phosphopantetheinyl transferase, ALDH1L2 – Aldehyde Dehydrogenase 1
37 Family Member L2, CoA – coenzyme A, DHRS2 – mitochondrial Dehydrogenase/Reductase
38 2, ETC – electron transport chain, FAS – fatty acid synthesis, FASN – fatty acid synthase,
39 LYRM – leucine tyrosine arginine motif, mtFAS – mitochondrial fatty acid synthesis, NAD^+ -
40 nicotinamide adenine dinucleotide (oxidized form), OGDH – oxoglutarate dehydrogenase,
41 PAGE – polyacrylamide gel electrophoresis, PDH – pyruvate dehydrogenase, PPT –
42 mammalian AASDHPPT, PPTase – phosphopantetheinyl transferase, PTM –
43 posttranslational modification, SDHB – succinate dehydrogenase subunit B, TCA –
44 tricarboxylic acid, VUS – variant of uncertain significance
45
46 **Main**
47 4'-phosphopantentheinylation is an essential post translational modification (PTM)
48 whereby a 4'-phosphopantetheine (4'PP) group, derived from coenzyme A (CoA), is covalently
49 attached to target proteins by a phosphopantetheinyltransferase (PPTase) enzyme[6]. A total of
50 six proteins in the mammalian proteome have been found to have a 4'-PP-modified serine:
51 three cytoplasmic proteins (Fatty Acid Synthase, FASN; Aminoadipate semialdehyde
52 dehydrogenase, AASDH; and Aldehyde Dehydrogenase 1 Family Member L1, AL1L1), and
53 three mitochondrial proteins (NADH:Ubiquinone Oxidoreductase Subunit AB1, NDUFAB1;
54 Aldehyde Dehydrogenase 1 Family Member L2, AL1L2; and mitochondrial
55 Dehydrogenase/Reductase 2, DHRS2)[6]. In mammalian genomes, however, there is only one
56 annotated PPTase: aminoadipate-semialdehyde dehydrogenase- phosphopantetheinyl
57 transferase (AASDHPPT), which was thought to exist solely in the cytoplasm[8]. It was therefore
58 unclear how 4'PP is attached to mitochondrial proteins.
59 Since no mammalian mitochondrial PPTase had ever been described, we questioned
60 whether an unidentified PPTase existed in mammals, or conversely if AASDHPPT (hereafter
61 abbreviated PPT) was important for mitochondrial function regardless of its reported
62 cytoplasmic localization. We therefore set out to understand if PPT was required for
63 mitochondrial function and, if so, how it modifies mitochondrial targets despite existing in
64 separate cellular compartments.
65 To test whether PPT is required for mitochondrial oxidative function, we used a
66 CRISPR/Cas-9-based strategy to mutate *Aasdhppt* in C2C12 mouse skeletal muscle
67 myoblasts. Complete loss of PPT was incompatible with growth, however we generated two
68 clonal cell lines with hypomorphic mutations in *Aasdhppt* (Extended Data Fig. 1A) that resulted

69 in decreased PPT expression (PPT-1 and PPT-2, Fig. 1A). We next asked whether PPT
70 deficiency resulted in altered respiratory-dependent growth by culturing cells in media with
71 either glucose or galactose, the latter requiring functional mitochondrial respiration. Clonal
72 mutant PPT-2 showed significantly reduced growth in glucose-containing media (Fig. 1B,
73 Extended Data Fig. 1B), while clonal mutant PPT-1 showed a modest, yet non-statistically
74 significant reduction in growth compared to control cells. In contrast, both PPT mutants
75 showed markedly reduced proliferation in galactose-containing media (Fig. 1C, Extended
76 Data Fig. 1B). We next performed a Seahorse mitochondrial stress test and observed that
77 PPT-deficient mutants exhibited a reduction in both basal respiration rate and spare
78 respiratory capacity compared to controls (Fig. 1D). To assess whether PPT-deficient
79 respiratory function was associated with perturbed OXPHOS complex expression and
80 assembly, we performed blue-native PAGE on isolated mitochondria from PPT-deficient and
81 control cells. PPT-deficient mutants displayed reduced levels of fully assembled ETC complex
82 I (CI), complex II (CII) and complex IV (CIV) (Fig. 1E). Complex V (CV) was largely unaffected.
83 Additionally, complex III (CIII) was not affected by PPT-deficiency but reductions in CIII-
84 containing supercomplexes (SC) were observed (Fig. 1E). Together, these data demonstrate
85 that PPT deficiency results in dysfunctional mitochondrial respiratory and ETC deficient
86 phenotypes.

87 Many ETC impairments affect mitochondrial metabolism by dysregulating the NAD^+/NADH
88 ratio, causing a disruption in TCA cycle flux and nutrient utilization. To assess the activity of
89 the TCA cycle we cultured cells in fully labeled ^{13}C-glutamine for up to 6 hours and evaluated
90 carbon entry into TCA cycle intermediates to assess reductive (blue) versus oxidative (red)
91 use of glutamine (Fig. 1F). At steady state, PPT-deficient cells demonstrated an increase in
92 the pool size of succinate and a decrease in downstream metabolites such as fumarate,
93 malate, and aspartate (Fig. 1G, Extended Data Fig. 1C-E). Pool sizes of citrate and α-
94 ketoglutarate were variable (Extended Data Fig. 1F and G); however, the ratio of malate to
95 citrate was consistently reduced in PPT mutants compared to controls (Fig. 1H). The reduction
96 of TCA metabolites downstream of succinate relative to citrate suggests a block in oxidative
97 (NAD^+ consuming) TCA cycle activity.

98 To assess whether this was indeed the case, we examined citrate labeling patterns.
99 Citrate M+4 results from the oxidation of glutamine to oxaloacetate and consumes NAD^+,
100 whereas Citrate M+5 results from the reductive carboxylation of glutamine to citrate and
101 regenerates NAD^+. PPT-deficient cells showed a reduction in M+4 citrate and an increase in
102 M+5 citrate compared to controls, indicating increased reductive carboxylation of glutamine

103 (Extended Data Fig. 1H). This is further supported by the increase in the ratio of citrate
104 M+5:citrate M+4 at isotopic steady state (Fig. 1I).
105 Citrate produced in the mitochondria can also be transported to the cytosol to be broken
106 down by ATP-citrate lyase (ACLY) into malate and acetyl-CoA, with citrate M+4 producing
107 malate M+4 and citrate M+5 producing malate M+3 (Fig. 1F). PPT-deficient cells displayed a
108 reduction in malate M+4, which likely results from the loss of M+4 citrate (Extended Data Fig.
109 1I). However, the PPT-deficient cells did not display a concordant increase in M+3 malate,
110 indicating that differences in malate labeling patterns result from mitochondrial malate, and
111 conversion of citrate to malate in the cytosol is similar or reduced in PPT mutants (Extended
112 Data Fig. 1I). In sum, the glutamine labeling patterns in PPT-deficient cells support a model
113 in which loss of oxidative metabolism in the mitochondria results in increased reductive
114 carboxylation of glutamine that is typical of cells with loss of ETC activity[14]. The finding that
115 malate M+3 is not increased in PPT-deficient cells also supports the notion that the reductive
116 carboxylation seen in PPT-deficient cells is driven by a need for NAD^+ regeneration and not
117 by a demand for cytoplasmic acetyl-CoA.
118 As *Aasdhppt* was clearly important for mitochondrial oxidative function, we next asked
119 which mitochondrial targets were likely to be most prominently involved in this phenotype. As
120 mentioned above, there are three known 4'PP-modified proteins in mammalian mitochondria,
121 NDUFAB1, AL1L2, and DHRS2[6]. To explore which of these putative targets displayed the
122 strongest genetic relationships to PPT, we analyzed gene co-dependency relationships from
123 the DepMap Public 23Q4+ Score Chronos dataset[15] to identify gene functionality within the
124 same biological pathway[16]. Among the three known mitochondrial 4'PP-modified proteins,
125 *AASDHPPT* gene effect was positively correlated only with *NDUFAB1* (Pearson r = 0.24)
126 (Extended Data Fig. 2A-C).
127 Unique among 4'PP-modified proteins, NDUFAB1 is a structural subunit of complex I of
128 the electron transport chain (ETC), as well as an integral part of the mitochondrial fatty acid
129 synthesis (mtFAS) pathway. mtFAS builds *de novo* fatty acyl chains on NDUFAB1, which are
130 required both as precursors for the biosynthesis of lipoic acid (LA), an important TCA cycle
131 enzyme co-factor, as well as to stabilize ETC assembly factors and iron-sulfur (FeS) cluster
132 biogenesis complexes via protein-protein interactions with NDUFAB1[12,13]. Because the newly
133 synthesized fatty acids are added to the terminal sulfhydryl group of the 4'PP PTM, the
134 addition of a 4'PP to NDUFAB1 is absolutely necessary for mtFAS to occur and to support
135 these downstream pathways[9]. Of note, the mtFAS pathway gene *OXSM* ranked third overall
136 for co-dependency with *AASDHPPT* (Pearson r = 0.42)[17] out of all genes in the Depmap

137 database (Extended Data Fig. 2D). Additional mtFAS pathway genes also ranked highly in
138 terms of *AASDHPPT* co-dependency, including *MCAT* and *MECR* (Pearson r = 0.36 and 0.32
139 respectively) (Extended Data Fig. 2E and F). Given that the 4'-PP modification is necessary
140 for acyl synthesis on NDUFAB1, these data suggested that impaired mitochondrial respiration
141 and TCA cycle metabolism in PPT-deficient cells is primarily attributable to altered mtFAS
142 function.

143 To further explore the genetic relationships between *AASDHPPT* and mtFAS, we
144 performed clustering and two-dimensional mapping of pairwise gene essentiality score
145 correlations with *AASDHPPT*. We included genes associated with the GO term "pantothenate
146 metabolism" from the DepMap project database as well as all genes encoding known
147 phosphopantetheinylated proteins, mtFAS pathway genes, and genes involved in downstream
148 lipoic acid synthesis and ETC assembly - such as the leucine, tyrosine, arginine motif (LYRM)
149 assembly factors which are regulated by mtFAS[13]. The analyzed genes grouped into four
150 distinct clusters based on gene essentiality (Extended Data Fig. 2G). Two-dimensional
151 mapping of correlation distance showed that *AASDHPPT* most strongly correlated with mtFAS
152 pathway genes, as well as several LYRM family members, further suggesting that PPT may
153 act as a critical regulator of mtFAS functional activity (Fig. 2A).

154 To test this hypothesis, we examined whether PPT-deficiency altered known mtFAS
155 pathway endpoints, including protein lipoylation and succinate dehydrogenase subunit B
156 (SDHB) stability, which is a reliable surrogate of the LYRM-dependent ETC assembly
157 mechanism we previously described[13]. PPT-deficient cells exhibited reduced lipoylation of
158 pyruvate dehydrogenase (PDH) and α-ketoglutarate dehydrogenase (OGDH) subunits (DLAT
159 and DLST, respectively) along with reduced stability of SDHB (Fig. 2B), resembling the
160 molecular phenotype of mtFAS-deficient cells.

161 Although one prior study demonstrated that PPT is able to add a 4'PP group to NDUFAB1
162 *in vitro*[8], its requirement for NDUFAB1 phosphopantetheinylation had never been tested in
163 any *in vivo* setting. We monitored 4'PP-modification of NDUFAB1 by immunoblot, as
164 unmodified apo-NDUFAB1 has a lower molecular weight and thus migrates faster than 4'PP-
165 modified holo-NDUFAB1[8]. As hypothesized, we found that apo-NDUFAB1 accumulated in
166 PPT-deficient cells while holo-NDUFAB1 was depleted, indicated by a downward shift on the
167 blot (Fig. 2B). PDH and OGDH lipoylation, SDHB stability, and detection of holo-NDUFAB1
168 were all rescued by transient re-expression of full length AASDHPPT with a C-terminal GFP-
169 Flag tag (PPT-GFP) compared to a control vector expressing mitochondrially localized DSRed
170 (mtDSRed) (Fig. 2C). Additionally, basal respiration and spare respiratory capacity were also

171 both restored by re-expression of PPT-GFP in both PPT-deficient cell lines (Fig. 2D). From
172 these data, we conclude that PPT is required for 4'-PP modification of NDUFAB1 and therefore
173 for downstream mtFAS activity, protein lipoylation, ETC assembly, and mitochondrial
174 respiration[11].

175 The question then became: if PPT is required for modification of mitochondrial proteins,
176 does it act in the cytoplasm, prior to mitochondrial import, or is there an undescribed
177 mitochondrial pool of PPT? To address this question, we performed immunofluorescence
178 staining for endogenous PPT and mitochondrial ATP synthase subunit ATP5a and assessed
179 co-localization (Fig. 3A, Extended Data Fig. 3A). As expected, PPT expression was
180 significantly reduced in PPT-deficient cells compared to controls, and exhibited a punctate,
181 perinuclear expression pattern that co-localized with ATP5a staining in control cells (Pearson
182 r = 0.60 and 0.62) (Fig. 3B, Extended Data Fig. 3B). Additionally, PPT expression was
183 surprisingly observed in the nucleus of some, but not all, cells; a finding that we did not pursue
184 further in the present study, but which raises intriguing questions for future work.

185 We further verified the observed mitochondrial localization using subcellular fractionation
186 and Western blotting in control and PPT-deficient cells. We detected endogenous PPT
187 expression in both mitochondria and post-mitochondrial supernatant (PMS)(Fig. 3C). PPT
188 expression was reduced in both fractions, and near-completely absent from mitochondria in
189 PPT-deficient cells (Fig. 3C). We also characterized subcellular localization of PPT-GFP, and
190 found strong signal overlap with ATP5a, in agreement with our endogenous immunostaining
191 observations (Fig. 3D).

192 We then asked whether this pool of mitochondrially-localized PPT was mitochondrially
193 associated or inside the mitochondrial matrix, where NDUFAB1 and the rest of the mtFAS
194 machinery reside. To tackle this question, we employed a bimolecular fluorescence
195 complementation (BiFC) system[21] to visualize the sub-mitochondrial localization of PPT. We
196 used a split-Venus tag system in which the N-terminus of the Venus fluorophore (VN, residues
197 1-172) was attached to either the N- or C-terminus of PPT, while the C-terminus of Venus (VC,
198 residues 155-238) was attached to the C-terminus of a control protein with known localization
199 (MFN2 or CS) or NDUFAB1. This system allows us to observe fluorescent signal only when
200 both halves of the split-Venus tag are able to associate within a compartment[21]. We quantified
201 Venus fluorescence in each of our BiFC conditions by flow cytometry, and found that in cells
202 expressing C-terminally tagged PPT (PPT-VN), significant Venus signal was only observed
203 when co-expressed with either CS-VC or NDUFAB1-VC (Fig. 3E-G, see Extended data Fig.
204 3C for gating strategy), indicating that PPT-VN does in fact localize to the mitochondrial matrix.

205 Most mitochondrial proteins are encoded by nuclear genes and are targeted to and
206 imported into mitochondria via an N-terminal mitochondrial targeting sequence (MTS),
207 consisting of approximately 20 to 40 amino acid residues[22]. Surprisingly, in contrast, cells
208 expressing N-terminally tagged PPT (VN-PPT), positive Venus fluorescence was only
209 detected when co-expressed with MFN2-VC (Fig. 3E-G), indicating that N-terminally tagged
210 VN-PPT is mitochondrially associated on the OMM. Because our BiFC data showed that
211 tagging PPT on the N-terminus prevented its localization in the mitochondrial matrix (Fig. 3E-
212 G), we hypothesized that mitochondrial localization of PPT may be driven by a N-terminal
213 MTS. To test this, we generated N-terminal truncations of PPT to the next two methionine
214 residues at positions 14 and 37 ($PPT_{\Delta 1\text{-}13}$-GFP and $PPT_{\Delta 1\text{-}36}$-GFP, respectively) and examined
215 their localization using fluorescence microscopy.
216 While PPT-GFP co-localized strongly with ATP5a, $PPT_{\Delta 1\text{-}13}$-GFP exhibited diffuse
217 localization throughout the nucleus and cytoplasm (Fig. 4A-B). $PPT_{\Delta 1\text{-}36}$-GFP exhibited weak
218 fluorescent expression mostly within the nucleus, suggesting that this larger N-terminal
219 truncation destabilizes PPT (Fig. 4A-B). Sub-cellular fractionation and Western blotting
220 supported our microscopy results, showing that while PPT-GFP and $PPT_{\Delta 1\text{-}13}$-GFP are both
221 present in post-mitochondrial supernatant (PMS) and mitochondrial fractions, $PPT_{\Delta 1\text{-}13}$-GFP
222 accumulates in the PMS (Fig. 4C), suggesting difficulty in localizing to mitochondria. We also
223 performed the converse experiment, in which we added only the first 36 amino acids of PPT
224 to GFP, to test the sufficiency of the putative MTS to drive GFP to the mitochondria
225 (PPT_MTS-GFP). PPT_MTS-GFP showed strong overlap with ATP5a staining by
226 fluorescence microscopy (Extended data Fig. 4A), as well as strong expression in the
227 mitochondrial fraction via Western blot (Extended data Fig. 4B), indicating that the first 36
228 amino acids of PPT comprise a bona fide MTS.
229 To test whether this newfound mitochondrial localization is required for PPT to modify
230 mitochondrial target proteins, we transduced PPT-deficient cells with mtDSRed, PPT-GFP,
231 $PPT_{\Delta 1\text{-}13}$-GFP, or $PPT_{\Delta 1\text{-}36}$-GFP, and assessed mtFAS pathway activity. Expression of PPT-
232 GFP rescued protein lipoylation and SDHB stability, whereas $PPT_{\Delta 1\text{-}13}$-GFP and $PPT_{\Delta 1\text{-}36}$-GFP
233 both failed to rescue either of these mtFAS-dependent endpoints (Fig. 4D). These data
234 demonstrate that mitochondrial localization of PPT is required for 4'PP-modification of
235 NDUFAB1. To further investigate whether mitochondrial localization of PPT is required for
236 OXPHOS activity, we performed growth assays as before in glucose- and galactose-
237 containing media, with cells PPT-deficient cells expressing mtDSRed, PPT-GFP, or $PPT_{\Delta 1\text{-}13}$-

238 GFP. We found that growth in galactose, which requires functional mitochondrial respiration,
239 was partially rescued by expression of PPT-GFP, and that $PPT_{\Delta 1\text{-}13}$-GFP rescued less well
240 than the full length PPT-GFP construct (Extended Data Fig. 4C-F). Together, these data
241 demonstrate that mitochondrial localization of PPT is necessary for phosphopantetheinylation
242 of NDUFAB1, mtFAS pathway activity, and respiration-dependent growth.

243 We recently described a pathogenic variant in the mtFAS gene *MCAT* c.812T>C; p.T271I
244 (rs760294168; NM_173467.4)[23]. As our data demonstrate that perturbed *Aasdhppt*
245 expression results in similar phenotypes as mtFAS loss, we wondered whether there may be
246 patients with pathological variants in *AASDHPPT*. We searched the ClinVar database[24] and
247 identified several missense variants of uncertain significance (VUS) in *AASDHPPT* that were
248 associated with suspected inborn genetic disease. We selected six of these variants for
249 analysis: c.343C>T; p.P12S (NM_015423.3), c.140G>A; pR47H (NM_015423.3), c.214G>T;
250 pA72T (NM_015423.3), c.235T>G; pW79G (NM_015423.3), c.247C>T; pR83C
251 (NM_015423.3), and c.286A>G; pK96E (NM_015423.3).

252 We created each of these missense mutations in our full length PPT-GFP construct and
253 assessed their ability to rescue perturbed mtFAS activity in our PPT-deficient cells. We found
254 that PPT-GFP R47H and PPT-GFP W79G exhibited weaker rescue effects compared to the
255 other variants (Fig. 4E, Extended Data Fig. 4G). In addition, cells expressing the PPT-GFP
256 W79G variant showed low levels of protein expression compared to the other variants, despite
257 expression from the same promoter (EF-1α promoter), suggesting that this variant may have
258 reduced protein stability. These data identify R47H and W79G as potential clinically observed
259 pathologic variants of *AASDHPPT*, with molecular phenotypes attributable to altered mtFAS
260 activity and perturbed cellular respiration.

261 Our data position PPT as a critical mediator of mitochondrial oxidative function, due to its
262 requirement for proper function of the mtFAS pathway. The discovery of distinct pools of PPT
263 raises questions about what factors control PPT activity in each compartment. For instance,
264 PPT uses CoA as the substrate for 4'PP-modification of target proteins. How perturbations in
265 CoA availability affect PPT enzymatic activity may have important implications for PPT targets
266 such as mtFAS in diseases with CoA dysregulation[15]. Moreover, our data demonstrate that
267 PPT is targeted to mitochondria via a N-terminal MTS, but how this localization is controlled
268 in cells to produce two distinct pools is completely unstudied. Whether PPT localization is
269 dynamic will also be an interesting and important area for future study. Of note, we identified
270 two probable pathogenic patient variants in *AASDHPPT*. Our results predict that patients
271 harboring these mutant alleles likely exhibit impaired mtFAS, leading to diminished

272 mitochondrial function. These data add to the growing list of patients with pathogenic variants
273 in mtFAS and lipoic acid synthesis genes and support the notion that impairments in CoA
274 metabolism may cause disease via mtFAS dysfunction[16,17].
275
276 **Methods**
277
278 ***Aasdhppt mutant cell lines, growth assays, and viral transduction***
279 C2C12 immortalized mouse skeletal myoblasts (ATCC CRL-1772, verification provided by
280 ATCC) were grown in DMEM supplemented with 4.5 g/L glucose, glutamine, and sodium
281 pyruvate (Corning, 10-013-CV) and 10% FBS (Sigma, F0926) in humidified tissue culture
282 incubators at 37°C, 5% CO_2. To generate *Aasdhppt* mutant clones, four sgRNA sequences
283 (**Table 1)** were designed targeting exon 1 or exon 2 of the mouse *Aasdhppt* gene and
284 subcloned into the pLentiCRISPR v2 vector using previously described methods[18]. Parental
285 C2C12s were transfected with pLentiCRISPRv2_sgAasdhppt or empty vector. 48 hours after
286 transfection, cells were sorted on GFP signal intensity and plated into 96-well plates to obtain
287 single cell colonies for expansion and establishment of stable, clonal cell lines. Clones were
288 screened for AASDHPPT protein expression levels and two control clones and two *Aasdhppt*
289 mutant clones were selected for further experiments. For growth assays 10,000 cells/well
290 were plated in 12-well plates or 1,000 cells/well in 48-well plates and grown in DMEM with
291 either no sodium pyruvate, 4 mM glutamine, and 25 mM glucose or no sodium pyruvate, 4
292 mM glutamine, and 10 mM galactose for 3 days in technical triplicates. Tissue culture plates
293 were placed in an IncuCyte® chamber (Sartorius) and percent confluency was measured from
294 sixteen, 10X magnification fields per well for 12-well plates, or nine, 10X magnification fields
295 for 48-well plates every 6 hours. For co-localization and rescue experiments, control and
296 *Aasdhppt* mutant clonal lines were transiently infected with retrovirus harboring a control
297 transfer plasmid expressing mtDSRed (pQXCIP mtDSRed) or pMMLV retrovirus vectors
298 custom designed, synthesized, and purchased from VectorBuilder (Chicago, IL, USA),
299 harboring full length, or N-terminal truncations of residues 1-13 or 1-36, of AASDHPPT with
300 C-terminal GFP and Flag tag- fusion. For generation of retrovirus constructs harboring single
301 point mutations in the full length AASDHPPT-GFP-Flag construct, primers in **Table 2** were
302 used with a New England Biolabs Q5 Site-Directed Mutagenesis Kit. Plasmid reactions were
303 transformed into competent *E. coli* and selected colonies were sequence validated for
304 successful incorporation of point mutations.
305

306 ***Genomic Sequence Analysis of AASDHPPT Mutants***

307 Approximately five million cells of each clonal mutant cell line, PPT-1 and PPT-2, were
308 pelleted and washed with PBS then frozen at -80ºC. Genomic DNA was extracted using a
309 column-based kit assay (Qiagen 69504). Aasdhppt was amplified using primers described in
310 **Table 3**, and sanger sequenced using the forward primer. Sanger sequencing peaks were
311 deconvoluted using the Indigo web-based software (https://www.gear-genomics.com)[19].

312

313 ***Crude mitochondrial isolation***

314 Cells were harvested and processed as previously described[13]. Briefly, cells were
315 harvested by trypsinization, washed once with cold, sterile PBS (Gibco, 10010-023), then
316 stored at -80°C. At the time of mitochondrial isolation, cell pellets were thawed and
317 resuspended in 1 mL CP-1 buffer (100 mM KCl, 50 mM Tris-HCL, 2 mM EGTA, pH 7.4)
318 supplemented with mammalian protease inhibitor cocktail (mPIC, Millipore Sigma P8340) and
319 mechanically lysed by 10 passes through a 1 mL insulin syringe with 26-guage needle and
320 centrifuged at 700 x g for 10 minutes to pellet unlysed cells and debris. Supernatant was
321 transferred to a new microcentrifuge tube and centrifuged at 10,000 x g for 10 minutes to
322 pellet the crude mitochondrial fraction. Post-mitochondrial supernatant (PMS) was used for
323 Western blot analysis or discarded. Mitochondrial pellets were resuspended in a small volume
324 of either RIPA buffer (10 mM Tris-HCl, pH 8.0, 1 mM EDTA, 0.5 mM EGTA, 1% Triton X-100,
325 0.1% Sodium Deoxycholate, 0.1% SDS, 140 mM NaCl) supplemented with mPIC, or CP-1
326 buffer, equal to approximately twice the pellet volume. Resuspended pellets were then used
327 for applications described below.

328

329 ***SDS-PAGE and immunoblotting***

330 Cultured cells were scraped from tissue culture plates directly into RIPA buffer
331 supplemented with mammalian protease inhibitor cocktail (mPIC, Millipore Sigma) and Pierce
332 Universal Nuclease, incubated at 4°C with constant agitation on a microcentrifuge tube orbital
333 shaker, then centrifuged at 17,000 x g for 20 minutes at 4°C to remove insoluble material.
334 Supernatant was then transferred to a new microcentrifuge tube to be saved as whole cell
335 lysate (WCL). For protein analysis, WCL, PMS, and/or crude mitochondrial fractions were first
336 normalized for total protein content via Pierce BCA Protein assay (Thermo Fisher Scientifc
337 23225). Samples were resolved by SDS-PAGE and transferred to nitrocellulose membranes.
338 Immunoblotting was performed using the indicated primary antibodies (**Table 4**) with

339 visualization and analysis of protein signal using Rabbit and Mouse IgG Antibody DyLight 680,
340 or 800, Conjugated secondary antibodies and Bio-Rad ChemiDoc Imaging System.
341
342 ***Seahorse Extracellular Flux Rate Assay***
343 Extracellular flux rate assays were performed on a Seahorse XFe96 Analyzer (Agilent).
344 Cells from the indicated clones were plated in approximately 22 wells of a 96-well seahorse
345 plate at a density of 10,000 cells/well in DMEM +10% FBS and allowed to adhere overnight.
346 The morning of the assay, cells were washed twice and media was replaced with non-buffered
347 seahorse media (Agilent 103680) supplemented with 25 mM glucose, 2 mM glutamine, and 1
348 mM sodium pyruvate. A standard mitochondrial stress test was then performed using 1 μM
349 oligomycin, 3 μM FCCP, and 0.5 μM Rotenone + 0.5 μM Antimycin A. Baseline oxygen
350 consumption was measured three times, followed by acute injection of oligomycin, followed
351 by FCCP and finally Rotenone + Antimycin A. Measurements were standard, with acute
352 injection of drug followed by 3 minutes of mixing then measurements of oxygen levels over 3
353 minutes, with three measurements per phase. Data were normalized with crystal violet
354 absorption for approximation of cell number. Results were analyzed in WAVE software.
355
356 ***Blue Native-PAGE***
357 Crude mitochondrial fractions were prepared and normalized for total protein content as
358 previously described. 100 μg of mitochondria were pelleted at 10,000 x g for 10 minutes at
359 4°C. Supernatant was removed and pellets were resuspended in 60 μL of 1x pink lysis buffer
360 (Invitrogen BN2003). Digitonin (GoldBio D-180-2.5) was added to samples at a final
361 concentration of 1% mass/volume and samples were incubated on ice for 15 min. Insoluble
362 material was pelleted by centrifugation at 17,000 x g for 20 minutes and supernatant was
363 transferred to new microcentrifuge tubes. 6 μL of NativePAGE sample buffer (Invitrogen
364 BN2004) was added to samples and 10 μL of sample (~15 μg of crude mitochondrial fraction)
365 was loaded per lane on pre-cast 3-12%, Bis-Tris NativePAGE gels (Invitrogen BN1001BOX)
366 with NativePAGE anode buffer (Invitrogen 2001) and dark blue cathode buffer (Invitrogen
367 BN2002) at 150V for 30-40 minutes then switched to light blue cathode buffer and run at 20
368 V overnight. Gels were then transferred to PVDF membranes at 100 V for 2 hours and blotted
369 with the indicated primary antibodies (**Table 4**. Secondary anti-mouse HRP antibody and
370 SuperSignal West Femto Maximum Sensitivity Substrate (Thermo Fisher Scientific 34096)
371 was used to visualize bands with a Bio-Rad ChemiDoc Imaging System.
372

373 ***Glutamine Tracing***

374 The indicated clonal cell lines were plated in 6-well plates in triplicate at a density of 200K
375 for PPT-1 and PPT-2, and 175K for Ctrl-1 and Ctrl-2 to account for differences in growth rate.
376 Cells were allowed to adhere for two hours, at which point the media was changed to
377 unlabeled media (Corning DMEM 17-207-CV with 1mM sodium pyruvate, 5mM glucose, and
378 4mM glutamine). After twenty hours in unlabeled media, wells were changed to labeled media
379 at the indicated time points prior to harvest (Corning DMEM 17-207-CV with 1mM sodium
380 pyruvate, 5mM glucose, and 4mM $U^{13}C$-glutamine). Three wells per cell line were left
381 unlabeled for natural isotope abundance correction, and another three per cell line were used
382 to determine cell number at the time of freezing. 24 hours after cells were in unlabeled media,
383 all wells were washed with normal saline once and frozen at -80°C. Plates were then extracted
384 for metabolites using a volume of 40:20:20 methanol:acetonitrile:water scaled to the number
385 of cells determined by the cell count wells (average from three wells). Lysates were sonicated
386 and incubated on ice for 60 minutes. At this point any insoluble material was spun out of the
387 sample at 17,000 x g for 10 minutes at 4°C. 1000 µL of supernatant was dried using a
388 SpeedVac concentrator. Dried metabolomics extracts were next resuspended in 100% water
389 containing 25 µg/mL D5-Glutamate (DLM-556, Cambridge) such that resuspension sample
390 equivalents were 5.82E+3 cells/µL. 2 µL of resuspended samples were injected on column, a
391 process blank was analyzed before and after experimental samples, and a pooled sample
392 was injected twice before experimental samples for column conditioning, and every 7-10
393 sample injections thereafter. Data dependent MS2 (ddMS2) data was collected from pooled
394 experimental replicates to identify group-specific compounds.

395 Data were collected on a Vanquish liquid chromatography system coupled to an Orbitrap
396 Exploris 240 (Thermo Fisher Scientific) using a heated electrospray ionization (H-ESI) source
397 in ESI negative mode. All samples were run through a 24-minute reversed-phase
398 chromatography ZORBAX extend-C18 column (1.8 µm, 2.1mm × 150mm, 759700-902,
399 Agilent, California, USA) combined with a guard column (1.8 µm, 2.1 mm × 5 mm, 821725-
400 907, Agilent). Mobile phase A was LC/MS H2O (W6-4, Fisher) with 3% LC/MS grade MeOH
401 (A456-4, Fisher), mobile phase B was LC/MS grade methanol (A456-4, Fisher), and both
402 mobile phases contained 10 mM tributylamine (90780-100ML, Sigma), 15 mM acetic acid,
403 and 0.01% medronic acid (v/v, 5191-4506, Agilent). For the re-equilibration gradient, mobile
404 phase A was kept the same, and mobile phase B was 99% LC/MS grade acetonitrile (A955-
405 4, Fisher). Column temperature was kept at 35ºC, flow rate 0.25 mL/min, and the solvent
406 gradient was as follows: 0-2.5 min held at 0% B, 2.5-7.5 min from 0% B to 20% B, 7.5-13 min

407 from 20% B to 45% B, 13-20 min from 45% B to 99% B, and 20-24 min held at 99% B. The
408 analytical solvent gradient was followed by a 16 min re-equilibration gradient to prep the
409 column before the next sample injection that went as follows: 0-0.05 min held at 99% B at
410 0.25 mL/min, 0.05-1 min from 99% B to 50% B and 0.25 mL/min to 0.1 mL/min, 1-11 min held
411 at 50% B and 0.1 mL/min, 11-11.05 min from 50% B to 0% B at 0.1 mL/min, 11.05-14 min held
412 at 0% B at 0.1 mL/min, 14-14.05 min held at 0% B and increased flow rate from 0.1 mL/min
413 to 0.25 mL/min, and 14.05-16 min held at 0% B and 0.25 mL/min. The mass spectrometer
414 acquisition settings were as follows: source voltage -2,500V, sheath gas 60, aux gas 19,
415 sweep gas 1, ion transfer tube temperature 320ºC, and vaporizer temperature 250ºC. Full
416 scan data were collected with a scan range of 70-800 m/z at a mass resolution of 240,000.
417 Fragmentation data was collected using a data-dependent MS2 (ddMS2) acquisition method
418 with MS1 mass resolution at 120,000, MS2 mass resolution at 15,000, and HCD collision
419 energy fixed at 30%.
420 Natural isotope abundance correction was done using the FluxFix Isotopologue Analysis
421 Tool*14* (version 0.1) web-based application[20]. Data analysis was conducted in Skyline (version
422 23.1.0.268), consisting of peak picking and integration, using an in-house curated compound
423 database of accurate mass MS1 and retention time derived from analytical standards and/or
424 MS2 spectral matches for the specified chromatography method.
425
426 ***AASDHPPT co-essentiality analysis and network modeling***
427 Gene essentiality scores and gene co-dependency Pearson correlation values were
428 obtained from the DepMap Portal Project Achilles 23Q4 release[9,21–23] in which genome-wide
429 CRISPR loss-of-function screens were performed in 1100 human cancer cell lines. Co-
430 Dependency plots between AASDHPPT and other genes were generated from gene
431 essentiality scores for each cancer line obtained directly from the DepMap Portal. For two-
432 dimensional network analysis, gene essentiality correlations for a custom list of genes were
433 used to create a data matrix (see Supplementary Excel File**)**. From this matrix, methodologies
434 and code originally published by Arnold et al.[24] and available at: https://github.com/finley-
435 lab/coessentiality-network were first used to generate a correlation matrix heatmap of
436 codependent gene modules. Co-dependent gene modules were then visualized as a network
437 diagram and genes with low correlation scores (Pearson $r < 0.2$) were filtered out as previously
438 described[24]. Graph edges were weighted according to the strength of pairwise gene
439 correlations.
440

441 ***Cell immunostaining and microscopy analysis***

442 Cells were seeded into chambered cover glass slides and cultured overnight. The
443 following day, cells were fixed in ice-cold 4% paraformaldehyde (PFA) in PBS solution for 10
444 minutes at room temperature, followed by 3 washes in 1X PBS solution. Cells were then
445 permeabilized and blocked in PBS solution containing 0.5% BSA, 5% goat serum, and 0.3%
446 Triton X-100 for 1 hour at room temperature. Cells permeabilized/blocked with blocking buffer
447 were then incubated with denoted primary antibodies overnight at 4°C followed by washes
448 with 1X PBS prior to incubation with Alexa Fluor conjugated secondary antibodies (**Table 4**)
449 for 2 hours at room temperature. Washes were repeated and cells were then stained with
450 Hoechst Dye for 10 minutes at room temperature. After subsequent washes, samples were
451 then imaged on a Zeiss LSM 880 with Airyscan and non-linear optics microscope, using a 40X
452 water objective and 1.2 NA to collect z-stacks.

453 For quantification of endogenous AASDHPPT expression in control and *Aasdhppt* mutant
454 clonal lines, regions of interest (ROIs) were manually drawn with Fiji software for individual
455 cells from channels with fluorescent ATP5a expression. Area was then measured for each
456 ROI with corresponding mean fluorescent intensity of signal from the AASDHPPT fluorescent
457 channel. Mean fluorescent intensity per cell area was then calculated. For statistical analysis,
458 GraphPad Prism v10 softwared was used to remove outliers from the data set by the ROUT
459 method, Q = 1%.

460 For colocalization analysis of endogenous AASDHPPT or AASDHPPT-GFP fusion
461 constructs with mitochondrial proteins in maximum intensity projections of each imaged field,
462 nuclear signal detected by Hoechst Dye staining was first used to create ROIs in Fiji. Pixels
463 with signal detected in nuclear ROIs in red and green channels were then removed from
464 images of the same field prior to merging of red and green channels so that colocalization
465 analysis would be exclusive of nuclei and limited to subcellular organelles and cytoplasmic
466 regions. Merged channels were then processed by the BIOP JACoP Fiji plugin
467 (https://c4science.ch/w/bioimaging_and_optics_platform_biop/image-
468 processing/imagej_tools/jacop_b/) using the Otsu method of thresholding for each channel to
469 generate Pearsons Correlation values.

470

471 ***Bimolecular fluorescence complementation (BiFC) assay***

472 To generate BiFC cell lines, five split-Venus constructs were designed and synthesized by
473 VectorBuilder in a pMMLV retroviral backbone. Constructs were designed to contain either the
474 C' terminal half of the Venus tag with blasticidin resistance (VC), or the N' terminal half of the

475 Venus tag with puromycin resistance (VN). VC constructs were tagged to the C' terminal end
476 of *citrate synthase* (CS-VC), *mitofusin 2* (MFN2-VC) or *Ndufab1* (NDUFAB1-VC). VN
477 constructs were tagged to either the C' or N' terminal end of *Aasdhppt* (PPT-VN and VN-PPT,
478 respectively). Following retroviral packaging in HEK293T cells, 40,000 wildtype C2C12 cells
479 were transduced to express either PPT-VN or VN-PPT in combination with each VC construct.
480 Negative control lines were generated by transducing cells with individual VC or VN constructs
481 alongside an empty vector control (PQXCIP for VC constructs, and PQXCIB for VN
482 constructs). This ensured that all cells were transduced with an approximately equal total viral
483 load. Stable populations were derived via combined puromycin and blasticidin selection (2
484 µg/mL each), yielding 11 cell lines in total; 6 with combined VC/VN constructs plus 5 single
485 construct controls.
486 For measurement of fluorescence, approximately 100,000 cells were trypsinized and
487 resuspended in 200 µL PBS. Cell suspensions were then assessment on an Accuri bench-top
488 cytometer, recording a minimum of 20,000 events per sample. The percentage of Venus-
489 positive cells was analyzed using FlowJo (v. 10.10.0). Fluorescence intensity histograms were
490 generated using FlowJo Layout Editor. A representative flow cytometry gating strategy is
491 shown in Extended data Fig. 3C. Visual confirmation of fluorescence achieved by imaging all
492 BiFC cell lines on a Nikon Eclipse Ti2 microscope. Briefly, 20,000 cells per cell line were
493 seeded in chamber cover slides (Cellvis, C4-1.5H-N). After 24 hours, cells were fixed in 4%
494 PFA for 30 mins at room temperature before imaging the following day (20X objective, 0.75
495 NA).
496
497 ***Statistics***
498 Statistical analysis was performed using GraphPad Prism 10. Unless otherwise noted,
499 data were analyzed by one-way ANOVA followed by two-sided Dunnett's multiple comparison
500 test (when compared to only control) or Šídák's or Tukey's multiple comparison test (when
501 comparing all groups). A p-value of <0.05 was considered statistically significant. Data that
502 included a third vairable (ex. time) was analyzed by two-way ANOVA followed by Tukey's
503 multiple comparison test.
504
505 **Table 1**

sgRNA cloned into pLentiCRISPRv2	sequence
PPT 1	GATGCGGTCTATCCAGCCGG
PPT 2	GCAGACGGATATGATCCCAA

PPT 3	AGCGGACCGAGCCGGTCGTA
PPT 4	GGAACACCATACGACCGGCT

506

507 **Table 2**

Primers for site-directed mutagenesis	**sequence**
P12S Fwd	GTGCGTGGTGAGCTCCATGGAGG
P12S Rev	AGCCTCTTAGCGGGG
R47H Fwd	GGAGAAGGAGCATATCGGCAAGTTC
R47H Rev	TCCGGCTGGATAGAC
A72T Fwd	GAAATTAGTTACCGAGAAATTGAATATCCC
A72T Rev	CTTATCATCAAACGACCAG
W79G Fwd	GAATATCCCTGGCGATCATATCCGTC
W79G Rev	AATTTCTCTGCAACTAATTTC
R83C Fwd	GGATCATATCTGCCTGCAGAGAAC
R83C Rev	CAAGGGATATTCAATTTCTC
K96E Fwd	GGTTCTTGCGGAAGACTCGTTGA
K96E Rev	GGCTTTCCCTTTGAAGTTCTC

508

509 **Table 3**

510

Primers for Genomic Amplification of *Aasdhppt*	
Forward Primer	TACCTGGCTTGAGGATCAGC
Reverse Primer	GGTTCTGCAGCAAGAACTGCAT

511

512

513 **Table 4**

Antibodies	**Source and reference number**
AASDHPPT	Proteintech 11244-1-AP
β-actin	Proteintech 66009-1-Ig
GRIM19	Abcam ab110240
SDHA	Abcam ab14715
UQCRFS1	Abcam ab14746

MTCO1	Abcam ab110270
ATP5a	Abcam ab14748
Lipoic acid	Millipore 437695
SDHB	Abcam ab14714
NDUFAB1	Abcam ab96230 and ab181021
GFP	Abcam ab290
Goat anti-Mouse IgG (H+L) AlexaFluor 568	Thermo Fisher A-11004
Goat anti-Rabbit IgG (H+L) AlexaFluor 568	Thermo Fisher A-11011
Goat anti-Mouse IgG (H+L), HRP	Thermo Fisher A28177
Goat anti-Mouse IgG (H+L) Dylight 800	Rockland Immunochemicals 610-145-002-0.5
Goat anti-Rabbit IgG (H+L) Dylight 800	Rockland Immunochemicals 611-145-002-0.5
Goat anti-Mouse IgG (H+L) AlexaFluor 680	Thermo Fisher A-21057
Goat anti-Rabbit IgG (H+L) AlexaFluor 680	Thermo Fisher A10043

Acknowledgments

This work was supported by funding from the NIH (R35GM151245 to SMN) and the Van Andel Institute – Metabolism & Nutrition (MeNu) Program. Stipend support for RJW and OAP was provided by the Van Andel Institute Graduate School (VAIGS). RW was also supported by NIH F30GM154476. We thank the Meijer Foundation for financial support of MC and EM. We also thank the Van Andel Institute's Flow Cytometry Core (RRID:SCR_022685) for their assistance with single cell sorting for generation of clonal cell lines, the Metabolomics and Mass Spectrometry Core (RRID:SCR_024903) for their assistance with labeled glutamine tracing experiments and analysis, the Optical Imaging Core (RRID:SCR_021968) for their assistance with airyscan microscopy, and the Bioinformatics and Biostatistics Core (RRID:SCR_024762) for their assistance with gene essentiality score correlation network analysis.

The authors declare no competing interests.

Data Availability

533 All data needed to evaluate the conclusions in the manuscript are present in the
534 manuscript and/or Supplementary Information. Additional data related to this paper may be
535 requested from the authors.
536
537 **Figure Legends**
538
539 **Figure 1. AASDHPPT is required for mitochondrial oxidative metabolism.**
540 (A) Whole cell lysates were immunoblotted for the denoted targets. Data are representative
541 of three biological replicates. (B-C) Cells were grown in either 25 mM glucose (B) or 10 mM
542 galactose (C) in an IncuCyte® system with images captured every 6 hours for 3 days. Data
543 represent the mean confluency; error bars denote SEM * = $p < 0.05$. ns = no significance. Data
544 are representative of 3 biological replicates (D) Seahorse mitochondrial stress test for Oxygen
545 Consumption Rate (OCR). Data are representative of three independent experiments. Error
546 bars represent SD. (E) Blue-native PAGE separation of isolated mitochondrial protein
547 complexes from denoted cell lines, followed by immunoblot with the indicated antibodies. Data
548 are representative of three biological replicates. (F) Schematic of isotopomeric labeling
549 patterns upon substitution of $U^{13}C$-glutamine for unlabeled glutamine. Open circles indicate
550 ^{12}C carbons, where circles with grey, red, or blue, indicate ^{13}C carbons. (G-H) Technical
551 triplicate samples (n=3) of the indicated cell lines cultured in $U^{13}C$-glutamine for the indicated
552 time points, harvested, and analyzed via LC-MS. Steady state metabolite pool sizes and ratios
553 are shown for the 4-hour labeling time point. (I) Ratio of Citrate M+5 to Citrate M+4 at the four-
554 hour time point. Error bars represent SEM (B, C), SD (D, G, H, I). * = $p<0.05$ ** = $p<0.01$, ***
555 = $p<0.001$, **** = $p<0.0001$ as determined by ANOVA followed by Tukey's multiple
556 comparisons test.
557
558 **Figure 2. AASDHPPT is required for mitochondrial fatty acid synthesis pathway**
559 **function.**
560 (A) Two-dimensional network diagram representing gene essentiality score correlations
561 between selected genes associated with *AASDHPPT* and known substrate targets, mtFAS
562 pathway members, LYRM family members, and the GO term "pantothenate metabolism" using
563 a minimum threshold correlation score > 0.2. Different colors represent genes associated with
564 clusters as shown in Extended Data Fig. 2G. Correlation strength is represented by the length
565 and thickness of the connecting edge. (B) Whole cell lysates immunoblotted for the denoted
566 targets. Data are representative of three biological replicates. # denotes non-specific bands.

567 Red asterisk denotes positive PPT expression band in clonal controls that is reduced in PPT-
568 deficient mutants. (C) Whole cell lysates from indicated cell lines expressing either mtDSRed
569 or PPT-GFP fusion protein were immunoblotted for protein expression of the denoted targets.
570 Data are representative of three biological replicates. (D) Seahorse standard mitochondrial
571 stress test to determine Oxygen Consumption Rate (OCR). Data are representative of three
572 independent experiments. Error bars represent SD.
573
574 **Figure 3. AASDHPPT localizes to the mitochondrial matrix.**
575 (A) Representative 40X HPF images of *Aasdhppt* mutant and control cell lines
576 immunostained with Hoechst dye to visualize nuclei and antibodies against AASDHPPT (red)
577 and ATP5a (green). Scale bars = 100μm. (B) Quantification of AASDHPPT and ATP5a signal
578 colocalization outside of the nucleus from n = 8 40X HPF per group assessed by Pearson's
579 correlation coefficient.(C) Subcellular fractionation of *Aasdhppt* mutant cell lines and control.
580 Post-mitochondrial supernatant (PMS) and mitochondrial lysate (Mito) was isolated from the
581 denoted cell lines and immunoblotted for AASDHPPT, ATP5a, and GAPDH. Data are
582 representative of three biological replicates. (D) Representative 40X HPF images of WT
583 skeletal muscle myoblasts expressing AASDHPPT-GFP (PPT-GFP) stained with Hoechst dye
584 and antibody against ATP5a (red). Scale bars represent 100 μm. Dashed outlines denote
585 magnified regions shown in panels with solid outlines. For all statistical analysis data represent
586 the mean; error bars denote SD. **** = $p<0.0001$ as determined by one-way ANOVA with
587 Šidák's multiple comparisons test. (E) Representative histograms of Venus (FITC)
588 fluorescence in the indicated BiFC cell lines. (F) Percentage of Venus-positive cells in the
589 indicated cell lines as measured by flow cytometry. Data represent the mean; error bars
590 denote standard deviation (n = 3 per group). Statistical significance was determined by one-
591 way ANOVA with Tukey's multiple comparison test. (G) Representative 20X images of
592 endogenous Venus fluorescence in VC + VN BiFC cell lines. Scale bars represent 50 μm.
593
594 **Figure 4. Mitochondrial AASDHPPT is required for mtFAS function.**
595 (A) Representative 40X HPF images of WT skeletal muscle myoblasts expressing
596 mtDSRed, PPT-GFP, 13 residue N-terminal truncation of PPT ($PPT_{\Delta 1\text{-}13}$-GFP), or 36 residue
597 N-terminal truncation of PPT ($PPT_{\Delta 1\text{-}36}$-GFP) constructs, stained with Hoechst dye and
598 antibody against ATP5a. Scale bars represent 100 μm. Dashed outlines denote magnified
599 regions shown in panels with solid outlines. Arrows denote weak expression of GFP signal
600 detected. (B) Quantification of PPT-GFP and ATP5a signal colocalization outside of the

601 nucleus from n = 8 40X HPF assessed by Pearson's correlation coefficient from experiment
602 shown in (A). Data represent the mean; error bars denote SD. **** = p<0.0001, determined
603 by one-way ANOVA with Dunnett's multiple comparisons test. (C) Subcellular fractionation of
604 WT cells expressing PPT-GFP, $PPT_{\Delta 1\text{-}13}$-GFP, or $PPT_{\Delta 1\text{-}36}$-GFP. Post-mitochondrial
605 supernatant (PMS) and mitochondrial lysate (Mito) was isolated from the denoted cell lines
606 and immunoblotted for the indicated targets. Blots are representative of three biological
607 replicates. (D) Whole cell lysates from cells expressing mtDSRed, PPT-GFP, $PPT_{\Delta 1\text{-}13}$-GFP,
608 or $PPT_{\Delta 1\text{-}36}$-GFP were immunoblotted for the denoted targets. Data are representative of n >
609 3 biological replicates. (E) Whole cell lysates from clonal control and *Aasdhppt*-deficient cells
610 transduced with retrovirus expressing mtDSRed, PPT-GFP P12S, PPT-GFP R47H, PPT-GFP
611 A72T, PPT-GFP W79G, PPT-GFP R83C, or PPT-GFP K96E were separated by SDS-PAGE
612 and immunoblotted for the denoted targets. Immunoblots are representative of three biological
613 replicates.
614
615 **Extended Data Fig. 1. AASDHPPT is required for mitochondrial oxidative metabolism.**
616 (A) Sequence analysis of sgRNA-targeted region in clonal Aasdhppt mutant cell lines, and
617 corresponding mutations generated. (B) Representative IncuCyte® phase contrast images
618 from cells denoted in Fig. 1B and C at 72 hours grown in glucose or galactose supplemented
619 DMEM. Scale bars represent 200 μm. (C-G) Pool size of the indicated metabolites from steady
620 state metabolomics analysis at the four-hour labeling time point. Data from n=3 technical
621 replicates of the indicated cell lines. Error bars represent SD. Statistical analysis was done
622 using a one-way ANOVA followed by Tukey's multiple comparisons test. (H-I) Fractional
623 enrichment of given isotopologues is represented as percentage of the total pool at each
624 indicated time point. Error bars represent SD. Significance was determined by two-way
625 ANOVA followed by Tukey's multiple comparisons test. ** = p <0.01. *** = p <0.001. **** = p
626 <0.0001. NS = not significant.
627
628 **Extended Data Fig. 2. AASDHPPT is required for mitochondrial fatty acid synthesis**
629 **pathway function.**
630 (A-F) Codependency plots of gene essentiality scores comparing *AASDHPPT* with
631 *NDUFAB1* (A), *ALDH1L2* (B), *DHRS2* (C), *OXSM* (D), *MCAT* (E), and *MECR* (F) from DepMap
632 CRISPR screens[9,21–23,25]**.** **(**G) Heatmap depicting hierarchical clustering of pairwise gene
633 essentiality score correlations of PPT, known PPT substrate targets, mtFAS pathway

634 members, LYRM family members, and genes associated with the GO term “pantothenate
635 metabolism.”
636
637 **Extended Data Fig. 3. AASDHPPT localizes to the mitochondrial matrix**
638 (A) Representative 40X HPF images of second clones of *Aasdhppt* mutants and controls
639 stained with Hoechst dye to visualize nuclei and antibodies against AASDHPPT (red) and
640 ATP5a (green). Scale bars = 100µm. (B) Quantification of mean fluorescent intensity of
641 AASDHPPT expression per cell area (μm^2) in *Aasdhppt* mutants (PPT-1 n = 170 and PPT-2
642 n =159) and control clonal cell lines (Ctrl-1 n = 186 and Ctrl-2 n = 118) as represented in (A
643 and Fig. 3A).
644
645 **Extended Data Fig. 4. Mitochondrial localization of AASDHPPT is required for mtFAS**
646 **function**
647 (A) Representative 40X images of cells expressing PPT_MTS-GFP stained with Hoechst
648 dye and antibody against ATP5a. Scale bars represent 20 μm. (B) Subcellular fractionation of
649 cells expressing PPT_MTS-GFP. Post-mitochondrial supernatant (PMS) and mitochondrial
650 lysate (Mito) was isolated and immunoblotted for the indicated targets. Blots are
651 representative of three biological replicates. (C,E) Cells were seeded in either 25 mM glucose
652 or 10 mM galactose and grown in an IncuCyte® system with images captured every 6 hours
653 for 3 days. Percent confluency measured by IncuCyte® software. Statistical analysis for
654 measurements at 72 hrs was performed with one-way ANOVA and Tukey’s multiple
655 comparisons test. * = $p < 0.05$. *** = $p < 0.001$. **** = $p < 0.0001$. Data presented are mean $\pm$
656 SEM from one experiment representative of three biological replicates. (D,F) Representative
657 IncuCyte® phase images from cells denoted in C and E at 72 hours grown in glucose or
658 galactose supplemented DMEM. Scale bars represent 200 μm. For all statistical analysis data
659 represent the mean; error bars denote SD. * = $p < 0.05$. ** = $p < .01$. **** = $p < 0.0001$, ns = not
660 significant as determined by one-way ANOVA with Dunnett’s multiple comparisons test. (G)
661 Whole cell lysates from second clones of control and *Aasdhppt*-deficient cells transduced with
662 retrovirus expressing mtDSRed, PPT-GFP P12S, PPT-GFP R47H, PPT-GFP A72T, PPT-GFP
663 W79G, PPT-GFP R83C, or PPT-GFP K96E were separated by SDS-PAGE and
664 immunoblotted for the denoted targets. Immunoblots are representative of three biological
665 replicates.
666
667

References

1. Chen, N., Liu, Y., Li, Y. & Wang, C. Chemical Proteomic Profiling of Protein 4'-Phosphopantetheinylation in Mammalian Cells. *Angew. Chem. Int. Ed Engl.* **59**, 16069–16075 (2020).
2. Joshi, A. K., Zhang, L., Rangan, V. S. & Smith, S. Cloning, Expression, and Characterization of a Human 4′-Phosphopantetheinyl Transferase with Broad Substrate Specificity*. *J. Biol. Chem.* **278**, 33142–33149 (2003).
3. Mullen, A. R. *et al.* Reductive carboxylation supports growth in tumour cells with defective mitochondria. *Nature* **481**, 385–388 (2011).
4. Tsherniak, A. *et al.* Defining a cancer dependency map. *Cell* **170**, 564-576.e16 (2017).
5. Wainberg, M. *et al.* A genome-wide atlas of co-essential modules assigns function to uncharacterized genes. *Nat. Genet.* **53**, 638–649 (2021).
6. Solmonson, A. & DeBerardinis, R. J. Lipoic acid metabolism and mitochondrial redox regulation. *J. Biol. Chem.* **293**, 7522–7530 (2018).
7. Nowinski, S. M. *et al.* Mitochondrial fatty acid synthesis coordinates oxidative metabolism in mammalian mitochondria. *Elife* **9**, e58041 (2020).
8. Van Vranken, J. G. *et al.* ACP Acylation Is an Acetyl-CoA-Dependent Modification Required for Electron Transport Chain Assembly. *Mol. Cell* **71**, 567-580.e4 (2018).
9. DepMap, B. DepMap 23Q4 Public. Figshare+ https://doi.org/10.25452/FIGSHARE.PLUS.24667905.V2 (2023).
10. Wedan, R. J., Longenecker, J. Z. & Nowinski, S. M. Mitochondrial fatty acid synthesis is an emergent central regulator of mammalian oxidative metabolism. *Cell Metab.* **36**, 36–47 (2024).
11. Kerppola, T. K. Design and implementation of bimolecular fluorescence complementation (BiFC) assays for the visualization of protein interactions in living cells. *Nat. Protoc.* **1**, 1278–1286 (2006).

694 12. Omura, T. Mitochondria-targeting sequence, a multi-role sorting sequence recognized at
695 all steps of protein import into mitochondria. *J. Biochem.* **123**, 1010–1016 (1998).
696 13. Webb, B. D. *et al.* Recessive pathogenic variants in MCAT cause combined oxidative
697 phosphorylation deficiency. *Elife* **12**, (2023).
698 14. Landrum, M. J. *et al.* ClinVar: improving access to variant interpretations and supporting
699 evidence. *Nucleic Acids Res.* **46**, D1062–D1067 (2018).
700 15. Naquet, P., Kerr, E. W., Vickers, S. D. & Leonardi, R. Regulation of coenzyme A levels by
701 degradation: the “Ins and Outs.” *Prog. Lipid Res.* **78**, 101028 (2020).
702 16. Kastaniotis, A. J., Autio, K. J. & R Nair, R. Mitochondrial fatty acids and neurodegenerative
703 disorders. *Neuroscientist* **27**, 143–158 (2021).
704 17. Lambrechts, R. A. *et al.* CoA-dependent activation of mitochondrial acyl carrier protein
705 links four neurodegenerative diseases. *EMBO Mol. Med.* **11**, e10488 (2019).
706 18. Sanjana, N. E., Shalem, O. & Zhang, F. Improved vectors and genome-wide libraries for
707 CRISPR screening. *Nat. Methods* **11**, 783–784 (2014).
708 19. Rausch, T., Fritz, M. H.-Y., Untergasser, A. & Benes, V. Tracy: basecalling, alignment,
709 assembly and deconvolution of sanger chromatogram trace files. *BMC Genomics* **21**, 230
710 (2020).
711 20. Trefely, S., Ashwell, P. & Snyder, N. W. FluxFix: automatic isotopologue normalization for
712 metabolic tracer analysis. *BMC Bioinformatics* **17**, 485 (2016).
713 21. Meyers, R. M. *et al.* Computational correction of copy number effect improves specificity
714 of CRISPR–Cas9 essentiality screens in cancer cells. *Nat. Genet.* **49**, 1779–1784 (2017).
715 22. Dempster, J. M. *et al.* Extracting biological insights from the project Achilles genome-
716 scale CRISPR screens in cancer cell lines. *bioRxiv* (2019) doi:10.1101/720243.
717 23. Dempster, J. M. *et al.* Chronos: a CRISPR cell population dynamics model. *bioRxiv*
718 (2021) doi:10.1101/2021.02.25.432728.

24. Arnold, P. K. *et al.* A non-canonical tricarboxylic acid cycle underlies cellular identity. *Nature* **603**, 477–481 (2022).

25. Pacini, C. *et al.* Integrated cross-study datasets of genetic dependencies in cancer. *Nat. Commun.* **12**, 1661 (2021).

FIGURE 1: AASDHPPT is required for mitochondrial oxidative metabolism

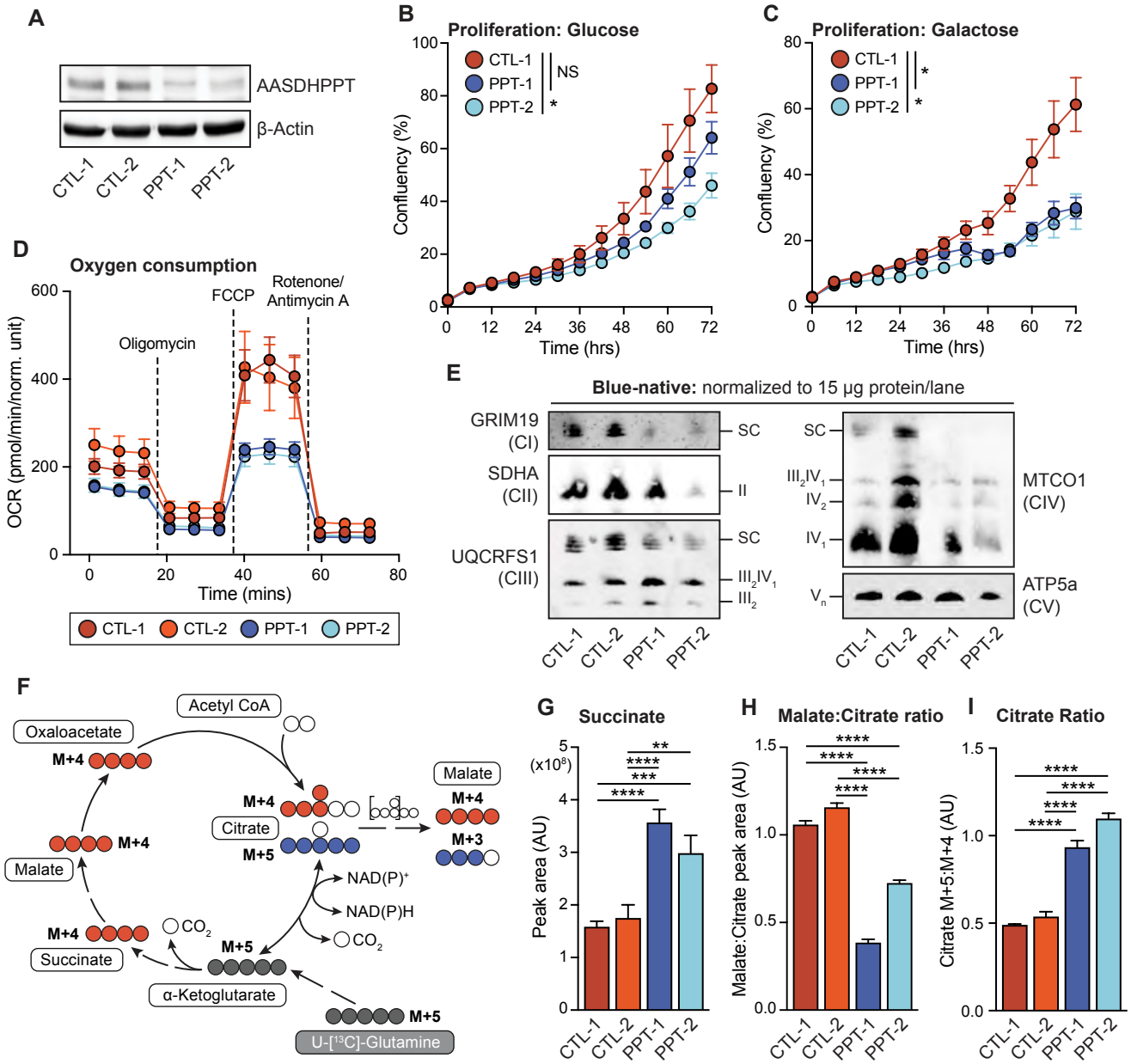

FIGURE 2: AASDHPPT is required for mtFAS pathway function

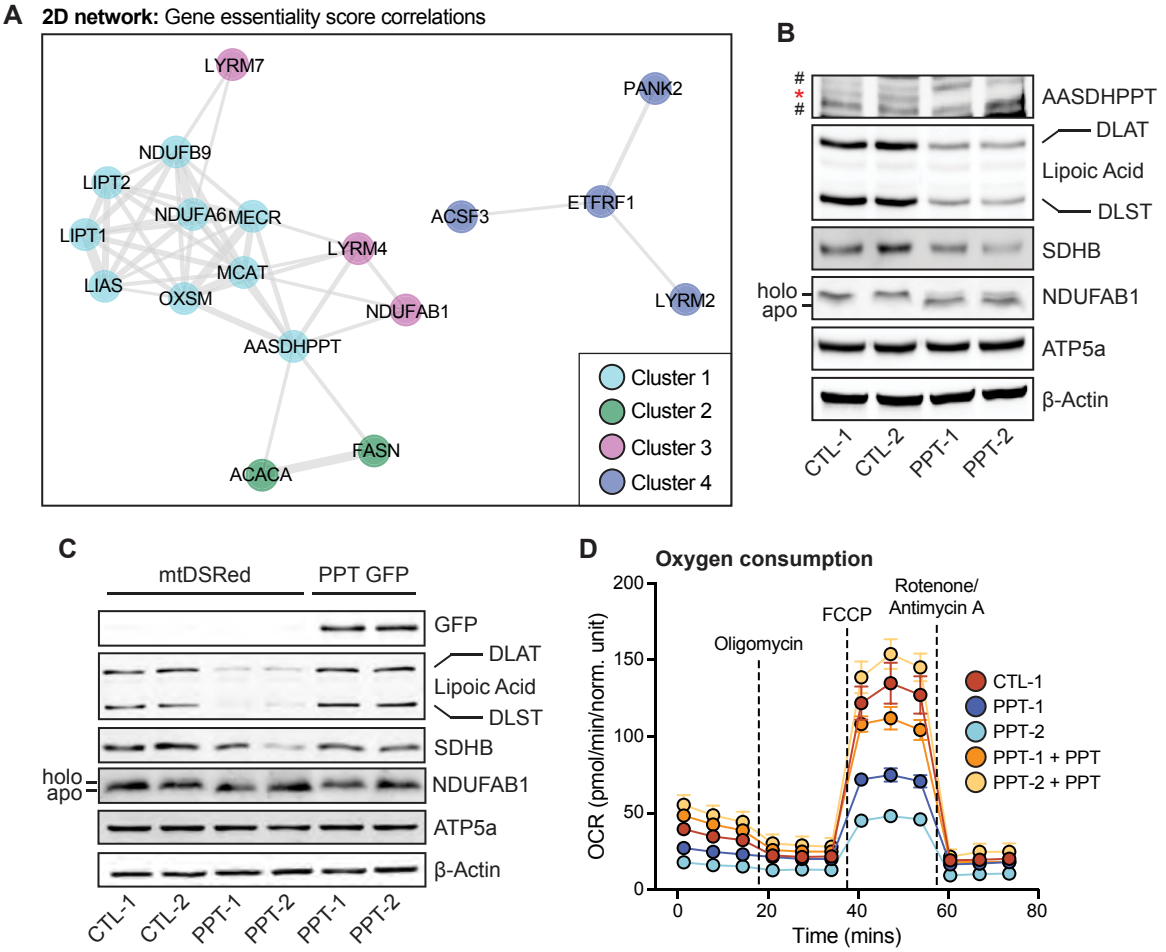

FIGURE 3: AASDHPPT localizes to the mitochondrial matrix

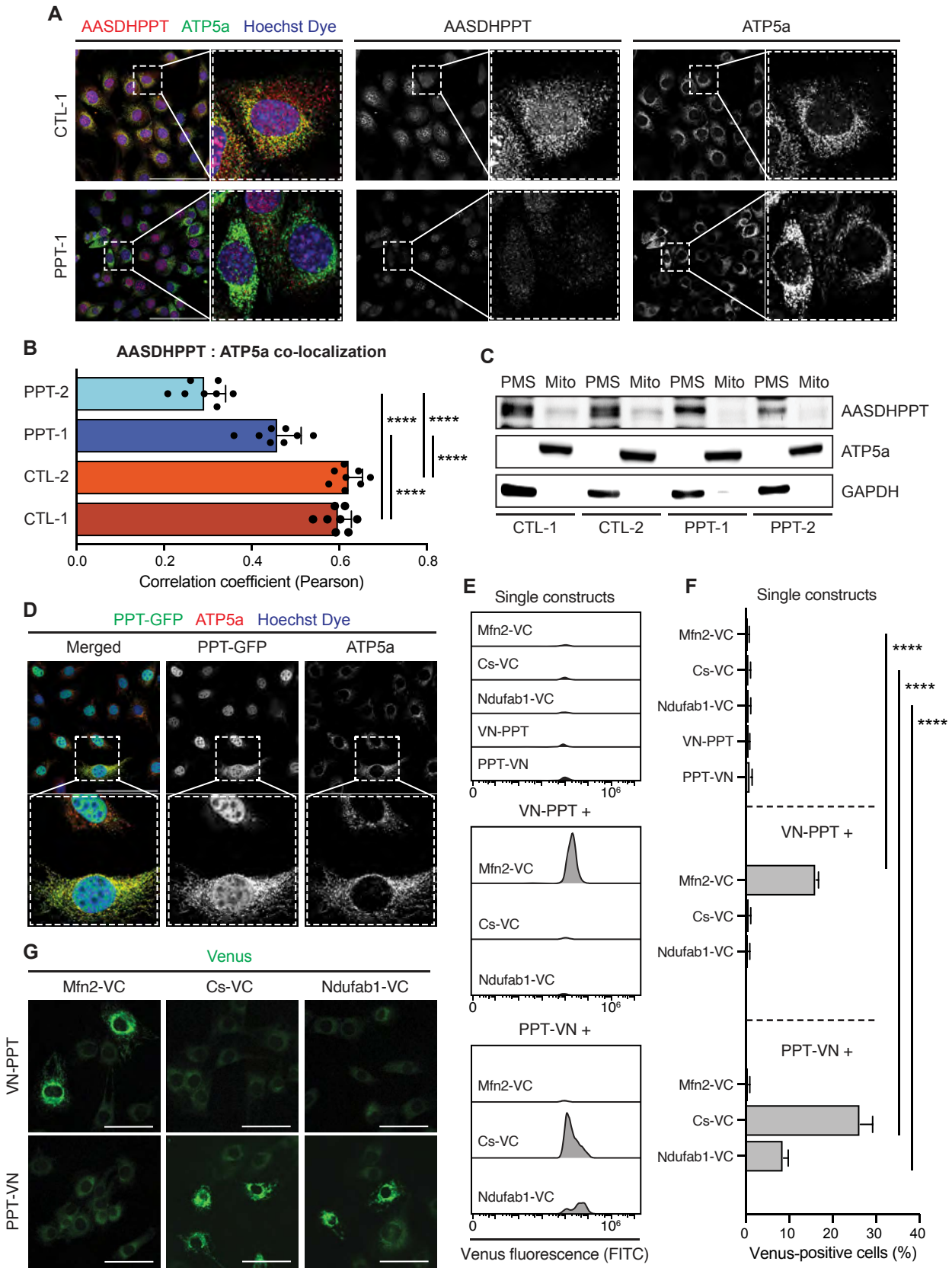

FIGURE 4: Mitochondrial AASDHPPT is required for mtFAS function

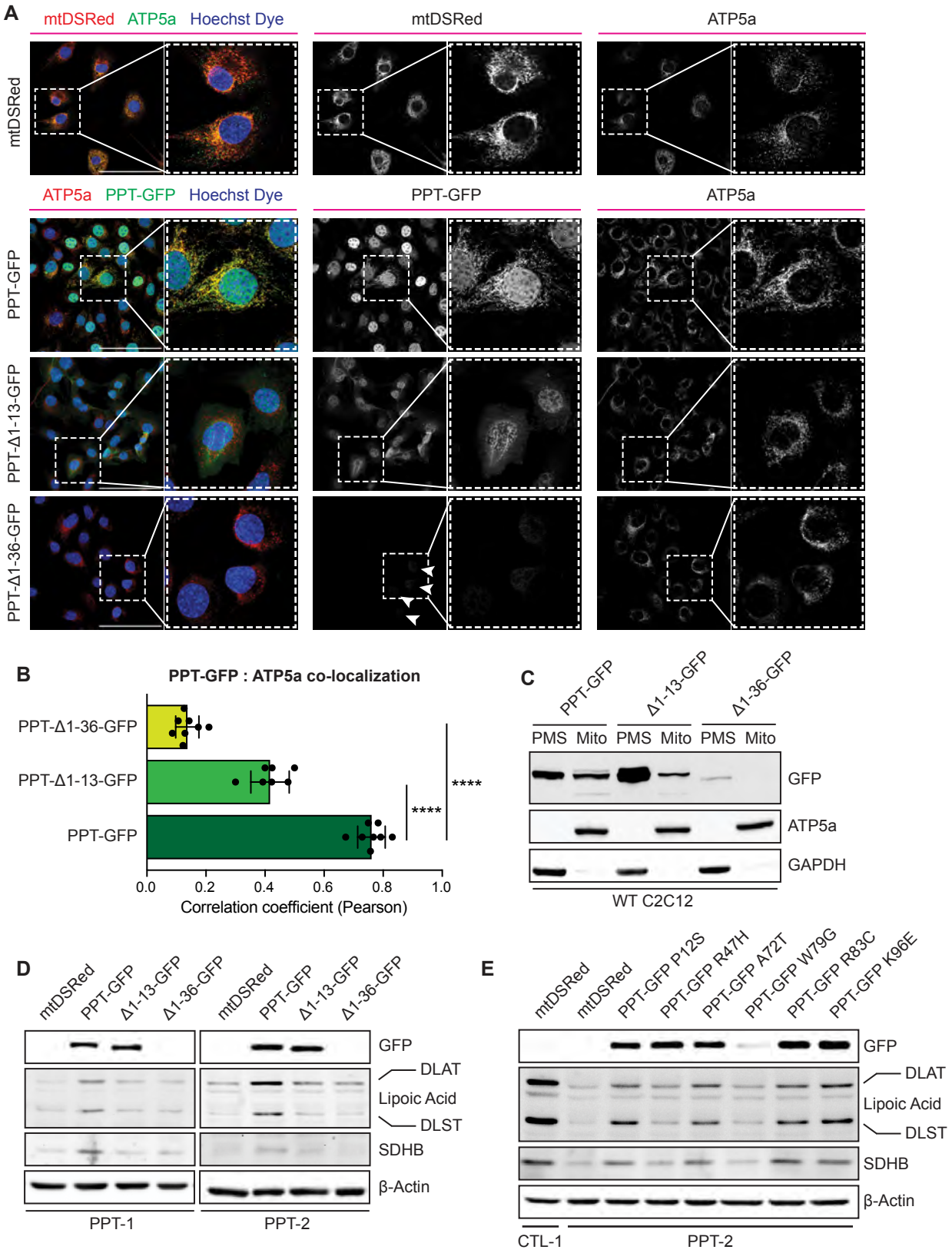

EXTENDED DATA FIGURE 1

A PPT-1/2 mutations

Cell line	NC_000075.7	Protein
PPT-1	c.342_344delAGC c.398G>C c.478C>G c.479T>G c.739C>T c.740T>G c.744C>T c.745G>T c.752G>A c.754T>A c.758G>A c.764A>T c.767Tdel c.771G>A c.773G>A c.779G>A	p.Q41del p.A60P p.A62G p.R64F p.M66I p.I67K p.L70F p.A72Q p.E73K p.K74N p.L75*
	c.342_346delAGCCG	p.0? (Frameshift)
PPT-2	c.366G>T c.394G>C c.757G>T c.771G>T	p.G49V p.K58N p.R68M p.E73*
	c.342_346delAGCCG	p.0? (Frameshift)

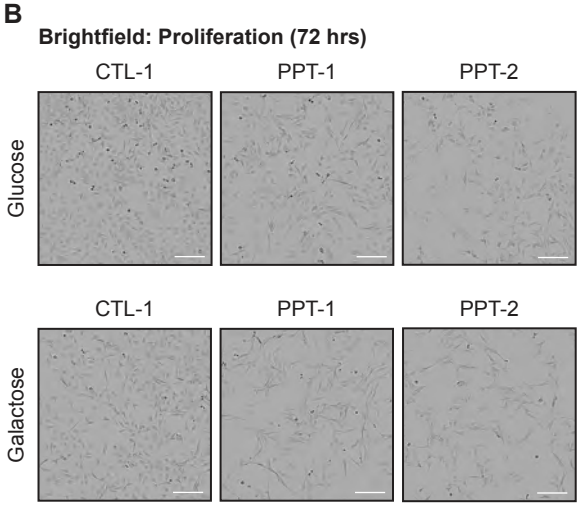

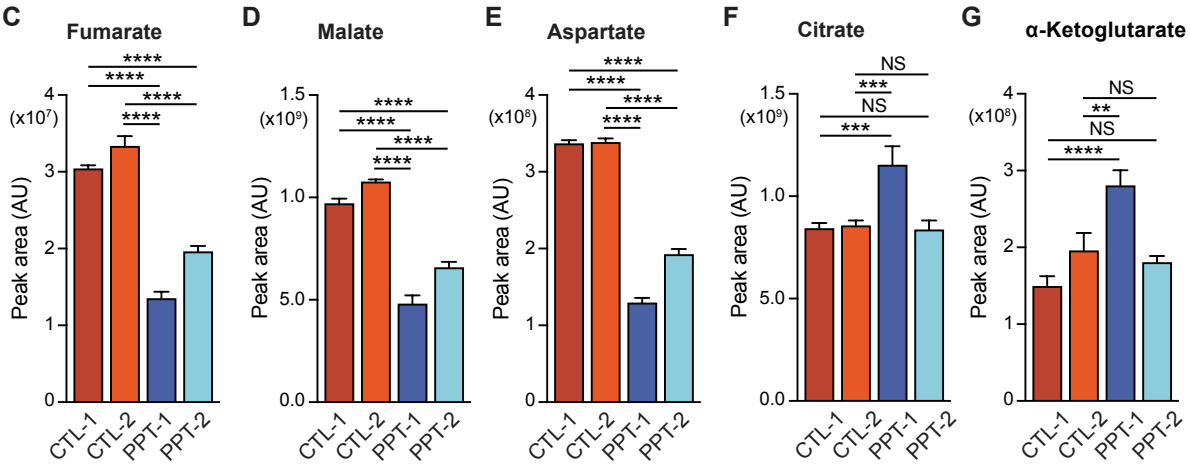

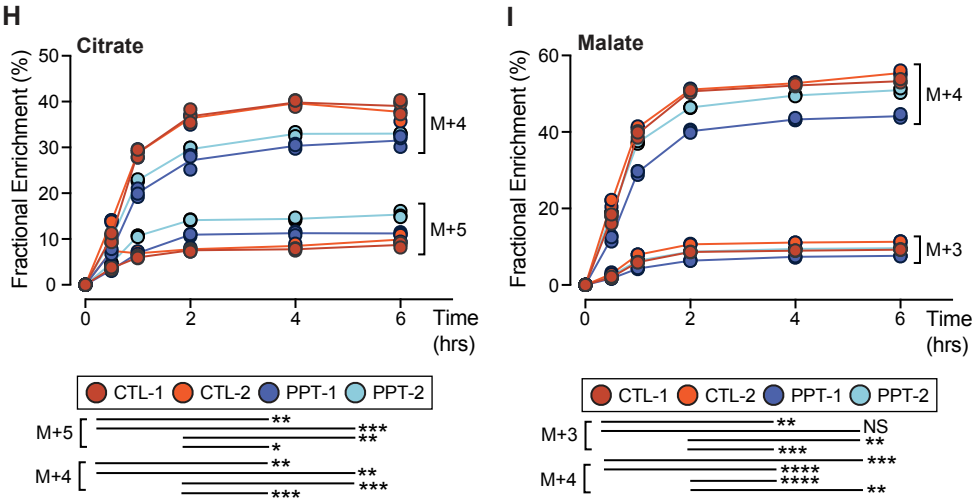

EXTENDED DATA FIGURE 2

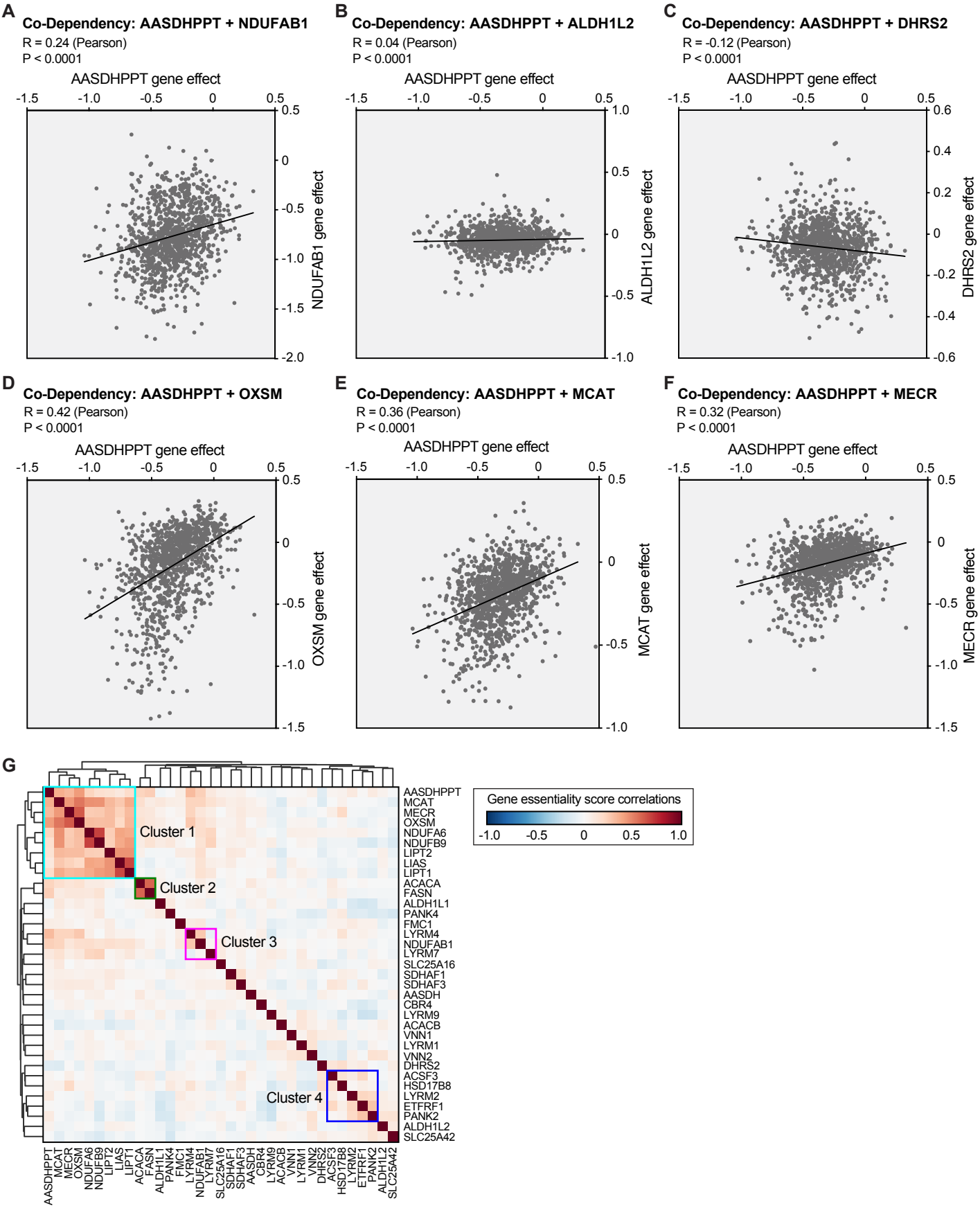

EXTENDED DATA FIGURE 3

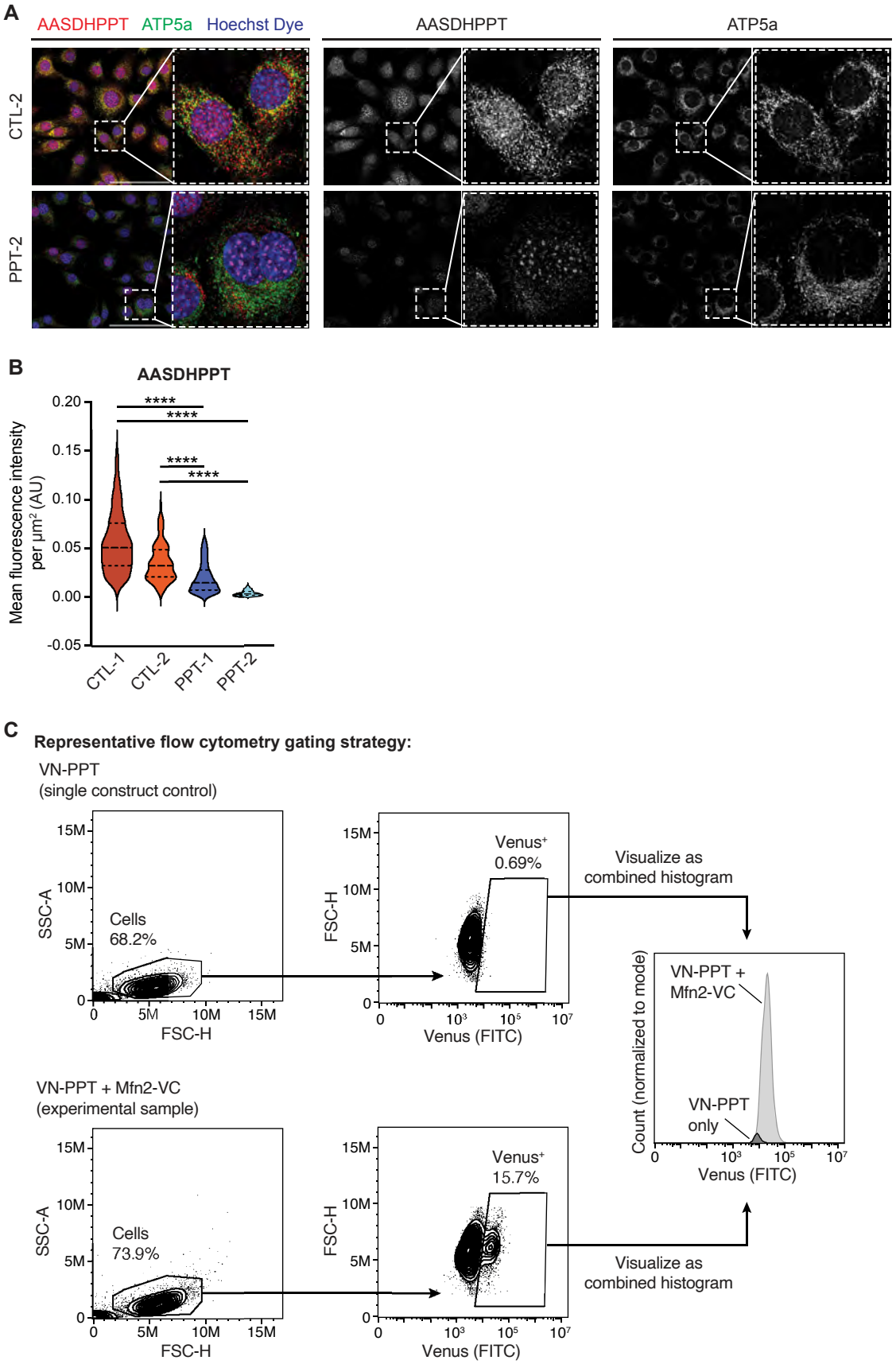
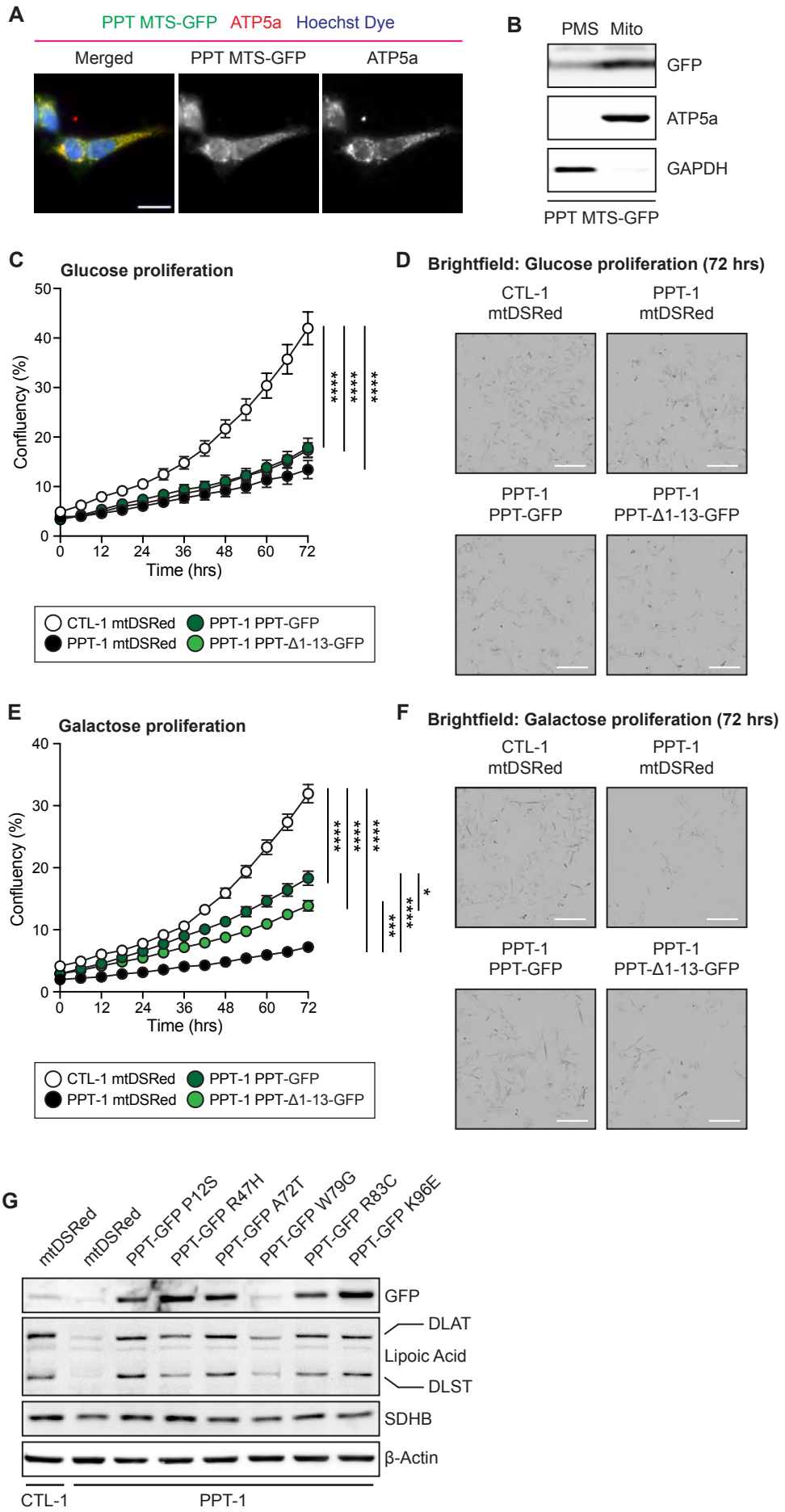
EXTENDED DATA FIGURE 4